NASA Technical Memorandum 4506

IN-02

209756

26 P

Computational Prediction of Isolated Performance of an Axisymmetric Nozzle at Mach Number 0.90
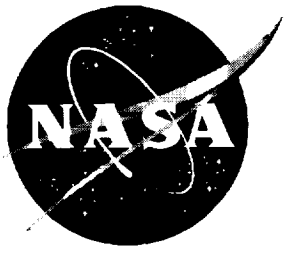
John R. Carlson

February 1994

Computational Prediction of Isolated Performance of an Axisymmetric Nozzle at Mach Number 0.90

John R. Carlson
Langley Research Center • Hampton, Virginia

Abstract

An improved ability to predict external propulsive performance has been incorporated into the three-dimensional Navier-Stokes code PAB3D. The improvements are the ability to account for skin friction and external pressure forces. Performance parameters for two axisymmetric supersonic cruise nozzle configurations were calculated to test the improved methodology. Internal and external flow-field regions were computed using a two-equation k-ε turbulent viscous-stress model. The computed nozzle discharge coefficient matched the experimental data within 0.5 percent in both level and trend. The calculated thrust-minus-drag ratios were within 1 percent of the absolute level of experimental data, and the trends of data were predicted accurately. The predicted trend of integrated nozzle pressure drag matched the trend of the integrated experimental pressure drag over a range of nozzle pressure ratios, but absolute drag levels were not accurately predicted.

Introduction

Highly maneuverable aircraft operate over a wide range of power settings and Mach numbers that require a propulsion system with variable geometry for obtaining efficient performance at different flight conditions. Understanding the effects of various nozzle geometries on the internal flow region and the surrounding boattail-nozzle region is vital for designing an efficient afterbody for these aircraft. The development and utilization of advanced computational methods will play a vital role in developing this understanding. Several on-going research activities currently exist at the Langley Research Center which are directed at establishing an experimental database for new nozzle concepts. Subsequent improvements to the computational methods are guided by these data.

A nozzle internal performance module (ref. 1) has been modified to include external aerodynamic effects. The module was incorporated into a Navier-Stokes solver PAB3D (ref. 2), which provides the flow-field solution. The nozzle performance module uses the control volume concept to calculate the body forces resulting from the fluid flow (ref. 3). Forces and moments are calculated from the integration of the momentum fluxes through the control volume faces. Skin friction on solid walls is calculated by using the gradient of the local velocity in the direction normal to the wall and the local viscosity. These calculations can be performed at intermediate steps throughout the solution procedure to provide an integrated flow quantity convergence in addition to monitoring the computational residuals in the flow solver algorithm.

This paper evaluates the module by using the data from the axisymmetric single-engine test body with jet-plume simulation reported in reference 4. Computed discharge coefficient, thrust-minus-drag ratio (measured axial force nondimensionalized by ideal isentropic thrust), and internal and external surface static pressures were compared with experimental data for a fixed free-stream Mach number of 0.90 at several nozzle pressure ratio settings for two of the nozzle concepts in reference 4.

Symbols

A_e	nozzle exit area, cm^2
$\mathbf{A}_{i,j}$	local rotation matrix
A_m	maximum cross-sectional area of model, 182.415 cm^2
A_t	nozzle throat area, cm^2
ΔA	incremental cross-sectional area, cm^2
$C_{D,\beta}$	boattail pressure-drag coefficient
C_d	discharge coefficient, $\frac{w_p}{w_i}$
$C_{F,i}$	aerodynamic ideal thrust coefficient, $\frac{F_i}{q_\infty A_m}$
$C_{p,\beta}$	boattail pressure coefficient
D_n	nozzle total drag, Pa
d_e	nozzle exit diameter, cm
d_m	model maximum diameter, 15.240 cm

d_t	nozzle geometric throat diameter, cm		γ	ratio of specific heats, 1.4 for air
e_{ij}	rate-of-deformation tensor		δ	nozzle divergence angle downstream of throat, deg
F	gross thrust along body axis, N		θ	nozzle convergence angle upstream of throat, deg
$\mathbf{F}$	total force vector, N			
F_i	ideal isentropic gross thrust along body axis, N		μ	viscosity, m^2/sec
			ξ_i	local Cartesian coordinate system on surface
i, j, k	indices, when associated with computational grid planes, denoting orientation in lateral, streamwise, and normal directions, respectively		ρ	density, kg/m^3
			τ_{ij}	viscous-stress tensor, Pa
			ϕ_i	local Cartesian skin friction force vector, N
l	axial length of boattail, cm			

Subscripts:

l_C	axial length of nozzle convergent section, cm		∞	free-stream conditions
l_D	axial length of nozzle divergent section, cm		flux	flux and pressure forces (flow-through face)
M	Mach number		pres	pressure forces (solid face)
$\mathbf{M}$	total moment vector, $N \cdot m$		fric	viscous forces (solid face)
$\hat{n}$	local surface normal vector in global system		ref	reference conditions
			local	local conditions

NPR   nozzle pressure ratio, $\frac{p_{t,j}}{p_\infty}$

Abbreviations:

NPR_{des}	design nozzle pressure ratio		A/B	afterburning
p	static pressure, Pa		C-D	convergent-divergent
$p_{t,j}$	jet total pressure, Pa		CFL	Courant-Friedrichs-Lewy
q	dynamic pressure, Pa		C2	configuration 2 of reference 4
R	gas constant ($\gamma = 1.4$), 287.3 $J/kg \cdot K$		C4	configuration 4 of reference 4
			2-D	two-dimensional
$\mathbf{R}$	moment arm vector, cm		3-D	three-dimensional

T	static temperature, K
$T_{t,j}$	jet total temperature, K

Experimental Model Configuration

General Model Description

$\mathbf{u}$	total velocity vector, m/sec
U_i	local Cartesian velocity, m/sec
w_i	ideal mass-flow rate, kg/sec
w_p	actual mass-flow rate, kg/sec
x	axial distance, positive downstream, cm
y^+	nondimensional distance from wall in turbulent boundary layer
α	angle of attack, deg
β	nozzle boattail angle, deg

    The experimental results selected for this computational study are reported by Carson and Lee in reference 4. A photograph of the model in the Langley 16-Foot Transonic Tunnel and a sketch of a representative test model and support system are presented in figures 1 and 2. The facility, which is a single-return, continuous-flow atmospheric wind tunnel with an octagonal slotted-throat test section, has a continuously variable Mach number range from 0.20 to 1.30. A detailed description of this wind tunnel is given in reference 5.

    The models of the axisymmetric, convergent-divergent (C-D) nozzles (figs. 3 and 4) had a circular-arc throat contour and conical divergent sections.

The nozzle geometries simulated a variable-geometry axisymmetric nozzle designed for a variable-cycle engine that was proposed for a supersonic cruise aircraft. Experimental data were obtained for five nozzle configurations that represented the geometries for different flight conditions and power settings. These geometries ranged from a subsonic cruise, dry power configuration, which would have a low expansion ratio and a high nozzle boattail angle, to a supersonic acceleration, maximum afterburning configuration, which would have a high expansion ratio and a low nozzle boattail angle. Tests were conducted at nozzle pressure ratios (NPR's) from jet off to approximately 10 at free-stream Mach numbers from 0.60 to 1.30. The nozzles were attached to an axisymmetric single-engine host body mounted on a sting-strut system and had a maximum cross-sectional area of 182.415 cm^2 (28.274 in^2). The ogive-shaped nose had an apex angle of 14° and a radius of curvature of 128.37 cm (50.54 in.). The nonmetric portion of the host body was 67.31 cm (56.50 in.) long. The model was cylindrical from the metric break to the nozzle connect station and was 69.85 cm (27.50 in.) long.

The jet was simulated by high-pressure air exiting the nozzle into the external free stream. An air system at the wind tunnel provides a continuous flow of clean, dry air at a stagnation temperature of nominally 300 K (540°R). The nozzle discharge coefficient was determined from experimentally measured jet total temperature, jet total pressure, and measured mass-flow rate. The thrust ratio was determined from the measured balance axial force that was nondimensionalized by the ideal thrust (determined from the measured nozzle mass flow) and corrected for internal pressure tare forces. Static pressure orifices were located on the external boattail and the internal nozzle surfaces.

Test Case Details

Two nozzle configurations from reference 4 were selected as test cases for the computational method, and they are described below.

Configuration 2. Configuration 2 of reference 4 is a high expansion ratio, axisymmetric, C-D nozzle. The external geometry is a circular-arc and straight-line type with a terminal boattail angle of 3.82°. The internal geometry has a circular-arc throat and a divergent section angle of 13.18° with an expansion ratio of 3.000 that results in a design NPR of 21.23. This geometry was chosen because the experimental data generally indicate no external flow separation at $M_\infty = 0.90$ for the NPR settings tested. In spite of the absence of data around the design NPR at $M_\infty = 0.90$ because of limitations in the attainable mass-flow rate of the experimental apparatus, it remains an interesting case for evaluation of a computational method. The internal flow does separate at lower NPR settings because of the high expansion ratio.

Configuration 4. Configuration 4 of reference 4 is a low expansion ratio, axisymmetric, C-D nozzle. The external geometry is a circular-arc and straight-line type with a terminal boattail angle of 8.28°. The internal geometry has a circular-arc throat and a straight-line divergent section angle of 4.78° with an expansion ratio of 1.500 and a design NPR of 6.23. This geometry was chosen because the experimental data were obtained around the design NPR and nozzle internal flow appears to remain attached at the lower NPR conditions because of the low expansion ratio.

Computational Procedure

Flow-Field Calculation

A three-dimensional Navier-Stokes code PAB3D was developed to predict the effects of the jet exhaust plume on nozzle-afterbody configurations. The thin-layer Navier-Stokes formulation (ref. 6) was modified to simulate jet mixing problems (ref. 2). The code allows for the discretization of the flow-field domain into multiblock grids and can utilize several numerical schemes to solve the governing equations and turbulence models as discussed in reference 7. The Roe upwind scheme with third-order accuracy is used to evaluate the explicit part of the governing numerical equations for relaxation in the streamwise direction, typically along the i index. The van-Leer scheme, with its faster convergence rate, is used to construct the implicit operator in the cross plane; typically this plane is a grid along the j and k indices. (Normally this code utilizes the Roe scheme to sweep streamwise through the computational domain and the van-Leer scheme for the solution of the cross plane.) For the present study, the streamwise grid plane is oriented along the j and k indices to take advantage of the implicit scheme for efficiency and accuracy. Solutions were developed using two versions of a two-equation k-ϵ turbulent viscous-stress model. A low Reynolds number k-ϵ model was used for the flow near solid surfaces while a high Reynolds number k-ϵ model was used in the regions of free-shear flow.

A user-written control file determines the communication between blocks and the type of boundary condition to be used at each face. Different grid

3

topologies for neighboring blocks and mixed boundary conditions on a block face are permitted, with some restrictions on grid matching at block boundaries. The code permits different numerical schemes to be selectively applied to each block.

Grid Definition

The block arrangement and dimensions of the grid are shown in figure 5(a). A sectional view of the overall grid in the j and k planes is shown in figure 5(b), and a sectional view of the two blocks defining the internal flow path is shown in figure 5(c). A 2-D wedge grid was used, and the flow was assumed to be axisymmetric. A single-cell-width cylindrical wedge grid was generated with a wedge angle of $5.00°$, which represents $1/72$ of an axisymmetric geometry.

The nozzle flow field was modeled by using five computational blocks. Two blocks represented the nozzle internal grid, and an additional two blocks represented the external grid region surrounding the nozzle. The fifth block modeled the external region downstream of the nozzle exit. The dimensions of the nozzle internal blocks were $2 \times 6 \times 49$ and $2 \times 78 \times 49$. The nozzle internal boundary-layer grid region contained approximately 24 points with the first grid point specified by $y^+ = 2.5$. The external blocks surrounding the nozzle grid were dimensioned $2 \times 6 \times 87$ and $2 \times 64 \times 87$. Approximately 40 streamwise grid points were used in the region of the nozzle boattail. The external downstream region, modeled by block 5, was dimensioned $2 \times 51 \times 135$. The interfaces matched point for point between the blocks upstream and downstream of the nozzle exit plane. The grid was extended to a distance of 15 nozzle exit radii away from the outer boundary. The outflow boundary was 5 exit radii downstream of the nozzle exit plane.

Boundary Conditions

The PAB3D code allows different boundary conditions to be applied to a given block face. Solid walls are treated as no-slip adiabatic surfaces. The inflow boundary conditions used for the internal nozzle flow path are the total pressure $p_{t,j}$ and the total temperature $T_{t,j}$. This particular inflow boundary condition assumes a fluid flow angle normal to the inflow face. The operating NPR of the nozzle and the free-stream static pressure p_∞ determines the jet total pressure $p_{t,j} = (\text{NPR})(p_\infty)$.

A jet total temperature of 300 K was used for all the calculations, and it was the nominal temperature set during the experimental investigation. The inflow Mach number, flow angle, total pressure, and total temperature were fixed along the external inflow

boundary. A boundary condition for Riemann invariants (ref. 2) along the characteristics was specified for the lateral free-stream boundary of the flow domain. An extrapolation boundary condition was applied on the downstream outflow face where both the external free stream and the nozzle plume stream exit the computational domain. The wedge-angle boundary condition determines the angle of the wedge lateral faces and the proper boundary values to apply for satisfying the symmetry assumptions. Flow properties were transferred between blocks through cell-by-cell conservation of the mass and momentum fluxes across the block interface with third-order continuity. However, some restrictions on the multiblock grid were expected by the code, such as an integer multiple to one correspondence between cells at the block interface and matched cell sizes in directions normal to the block interface.

Performance Calculation

Nozzle performance is obtained through the application of the momentum theorem to a control volume surrounding the nozzle (ref. 3). Cheatham, Walker, and Gridley calculated both 2-D and 3-D inviscid nozzle performance in reference 8, and Carlson calculated 3-D viscous nozzle performance in reference 1 by using the control volume method. Integration of the flow quantities is typically performed across the nozzle exit. The method integrates the mass and momentum fluxes and the pressure forces over each cell by using equations (1) and (2) for flow-through sections of the control volume:

$$w_p = \sum (\rho \mathbf{u} \cdot \hat{\mathbf{n}}) \, \Delta A \qquad (1)$$

$$\mathbf{F}_{\text{flux}} = \sum [\rho \mathbf{u}(\mathbf{u} \cdot \hat{\mathbf{n}}) + (p - p_\infty)\hat{\mathbf{n}}] \, \Delta A \qquad (2)$$

where ΔA is the incremental cross-sectional area of the cell face and $\mathbf{R}$ is the moment arm vector from the reference center to the cell face.

Ideal mass-flow rate and thrust are determined from the isentropic flow equations (3) and (4), respectively (ref. 9), and they are used to normalize the calculated mass-flow rate and thrust for comparisons with the experimental data:

$$w_i = \sqrt{\frac{\gamma}{R}} \left(\frac{2}{\gamma + 1}\right)^{\frac{\gamma+1}{2(\gamma-1)}} A_t \frac{p_{t,j}}{\sqrt{T_{t,j}}} \qquad (3)$$

$$F_i = \sqrt{\frac{2\gamma R}{\gamma - 1}} \, w_p \sqrt{T_{t,j} \left[1 - \left(\frac{p_\infty}{p_{t,j}}\right)^{\frac{\gamma-1}{\gamma}}\right]} \qquad (4)$$

4

Skin friction and pressure forces are calculated for solid wall sections of the control volume. The solid surface pressure force is calculated by extrapolating the cell centered static pressure to the surface wall and multiplying this pressure by the cell face area:

$$\mathbf{F}_{\text{pres}} = \sum \left[(p - p_\infty)\hat{\mathbf{n}} \right] \Delta A \qquad (5)$$

The viscous-stress tensor used for determining the skin friction force is calculated by using only the velocity derivatives normal to the surface. The velocity gradients are determined by a two-point difference. The first velocity is a zero magnitude vector positioned on the surface. The second velocity is the velocity at the cell center as sketched in figure 6. Equations (6a) and (6b) are two of the nonzero components of the rate-of-deformation tensor calculated (ref. 10):

$$e_{13} = \frac{\partial U_1}{\partial \xi_3} \qquad (6a)$$

$$e_{23} = \frac{\partial U_2}{\partial \xi_3} \qquad (6b)$$

where $U_i = \mathbf{A}_{ij}\mathbf{u}_j$. The remaining velocity derivatives are assumed to be zero. The set of local velocity components U_i are in a local surface Cartesian coordinate system ξ_i (where ξ_3 is the direction normal to the surface), which is determined from an orthogonal transformation of the global velocity components by the rotation matrix $\mathbf{A}_{ij}$. In general $e_{ij} = \frac{\partial U_i}{\partial \xi_j}$, where $i \neq j$.

The local shear-stress tensor τ_{ij}, where $i \neq j$, was the local viscosity multiplied by the velocity gradients e_{ij}, where $i \neq j$. The viscosity was determined from Sutherland's formula (ref. 11) by using the static temperature at the local cell center:

$$\mu_{\text{local}} = \mu_{\text{ref}} \left[\frac{(T_{\text{ref}} + 110.33)}{(T_{\text{local}} + 110.33)} \right] \left(\frac{T_{\text{local}}}{T_{\text{ref}}} \right)^{1.50} \qquad (7)$$

$$\tau_{ij} = \mu_{\text{local}} e_{ij} \qquad (i \neq j) \qquad (8)$$

The local skin friction force components ϕ_i were

$$\phi_i = (\tau_{ij}\mathbf{n}_i) \Delta A \qquad (9)$$

where $\mathbf{n}_i$ is the ith component of the unit normal vector $\hat{\mathbf{n}}$ and ϕ_i were transformed back to a force vector expressed in global coordinates $\mathbf{F}_{\text{fric}}$. The solid surface forces are then added to $\mathbf{F}_{\text{flux}}$ for the total volume forces:

$$(\mathbf{F}_{\text{fric}})_j = \phi_i \mathbf{A}_{ij}^T \qquad (10)$$

$$\mathbf{F} = \mathbf{F}_{\text{flux}} + \mathbf{F}_{\text{pres}} + \mathbf{F}_{\text{fric}} \qquad (11)$$

The performance package is incorporated into PAB3D to permit monitoring of various performance parameters as the solution convergences.

Discussion of Results

Experimentally measured external-surface static-pressure coefficient distributions and the internal-surface pressure ratio distributions are compared with calculations in figures 7 to 12. Various measured force parameters are compared with calculations in figures 13 to 17. Specific comparisons are presented in the following figures:

Discussion

Solutions were obtained for two nozzle configurations by using the PAB3D flow solver. The solutions were computed by using a single-cell-width 2-D mesh oriented so that the entire flow field was solved implicitly with each iteration. All solutions were developed by using a two-equation, k-ϵ turbulent viscous-stress model. Discharge coefficient, ideal thrust coefficient, thrust-minus-drag ratio, and nozzle drag coefficient were calculated for different nozzle operating conditions, which exhausted into a $M_\infty = 0.90$ free-stream airflow at an angle of attack of 0°. The calculations are summarized as follows:

Parameter	NPR			
	4	5	6	7
Configuration 2				
Iteration	8000	6800	2000	2500
Computer time, hr .	3.3	2.8	0.8	1.0
C_d	0.963	0.963	0.963	0.963
$(F - D_n)/F_i$	0.789	0.787	0.849	0.887
Configuration 4				
Iteration		2500	2500	1500
Computer time, hr .		1.0	1.0	0.6
C_d		0.966	0.966	0.966
$(F - D_n)/F_i$		0.969	0.979	0.984

The solutions started with a CFL number of 1. The CFL number for subsequent iterations during a run were adjusted automatically within the code for convergence acceleration. Flow solution residuals, discharge coefficient, thrust ratio, and nozzle drag were obtained at regular intervals during the solution development. Typical solution convergence criteria are less than 0.05 percent change in discharge coefficient, less than 0.1 percent change in thrust ratio, and less than 0.001 change in nozzle drag coefficient over the previous 1000 iterations. Solutions with flow separation typically required an additional 3000 to 4000 iterations beyond the average 1500 to 3500 iterations to establish an acceptable level of performance convergence. Situations of flow instability because of either real flow physics or numerical modeling difficulties occasionally caused some performance parameters to oscillate about a median value. The solutions for this study met the general convergence criteria with little or no occurrence of oscillations in performance numbers.

Comparisons of predicted internal and external static pressure distributions with experimental data are made for configuration 2 at NPR = 4, 5, and 6. Predicted static pressure distributions are compared with experimental data for configuration 4 at NPR = 5, 6, and 7. Predicted performance parameters are compared with experimental data.

Static-Pressure Comparisons

Computed external and internal static-pressure distributions are compared with experimental data for configuration 2 in figures 7 to 9. In general, the external static-pressure coefficients are matched well for all three NPR conditions tested (figs. 7(a), 8(a), and 9(a)). The corner flow expansion near $\frac{x}{d_m} = 0$ is slightly overpredicted and the trailing-edge flow

expansion is slightly low, which is possibly a result of grid density in those locations. The flow separation over the internal divergent section near $\frac{x}{d_m} = 0.7$ is fairly closely matched (fig. 7(b)) at NPR = 4. Neither the apparent internal flow separation at NPR = 5 (fig. 8(b)) at $\frac{x}{d_m} = 0.92$ nor the trailing-edge flow compression at NPR = 6 (fig. 9(b)) at $\frac{x}{d_m} = 0.995$ was predicted. Extremely fine grid in the vicinity of the nozzle trailing edge in the external and internal regions would probably be required to resolve such detailed local flow structure. The slight mismatch of the computed pressures and the experimental data upstream of $\frac{x}{d_m} = 0.20$ is probably because of a geometry documentation difficulty in reference 4. Analytic results performed in reference 4 and the present method showed very similar trends in the internal static-pressure distributions in the region upstream of the throat.

Computed external and internal static-pressure distributions for configuration 4 are compared with experimental data in figures 10 to 12. The predicted external pressure-coefficient distributions match well with experimental data except for the magnitude of the flow expansion around the circular-arc closure of the boattail $\left(0 < \frac{x}{d_m} < 0.2\right)$ in figures 10(a), 11(a), and 12(a). The overprediction of this flow acceleration is, again, possibly because of grid density in that region of the model. The internal flow for this nozzle remained fully attached for the range of NPR examined. The internal static-pressure ratio distribution downstream of the throat typically changed little for choked nozzle flow that filled the internal nozzle volume completely. The solutions matched the experimental internal pressure distributions closely for the three NPR computed and shown in figures 10(b), 11(b), and 12(b) (NPR = 5, 6, and 7, respectively).

Performance Comparisons

Figures 13 to 16 show comparisons of computed performance parameters with experimental data from reference 4. All data were at a free-stream Mach number of 0.90 and a free-stream angle of attack of 0°. Additional experimental data were plotted to show general trends that surrounded the conditions chosen for the analytic study.

Discharge coefficient. A comparison of predicted discharge coefficients with experimentally determined discharge coefficients is shown in figure 13. The experimental data, shown by the circle and square symbols, were obtained at static conditions. Theoretically, external flow has no effect on

discharge coefficients once the internal flow is choked (NPR > 1.89). Thus, a comparison of computed discharge coefficients at $M_\infty = 0.90$ with experimental discharge coefficients at $M_\infty = 0.0$ is valid. The predicted discharge coefficients for configuration 2 are within 0.5 percent of the experimental data. The predicted discharge coefficients for configuration 4 are within 0.1 percent.

Ideal thrust coefficient. Predicted ideal thrust coefficients for both configurations are compared with experimental data in figure 14. The ideal thrust coefficient is the ideal nozzle thrust nondimensionalized by using the free-stream dynamic pressure q_∞, a reference area A_m, and the physical mass flow w_p. This coefficient is used as a means of converting aerodynamic coefficients normalized by $q_\infty A_m$ to propulsive-force ratios based on F_i. For these configurations, the reference area is the maximum cross-sectional area of the model. The ability to predict this quantity should be similar to the ability to predict the discharge coefficient. In general, the level and slope of the computed ideal thrust coefficient and the experimental data are closely matched, which indicates that the trends in the mass flow with NPR were predicted properly.

Aeropropulsive performance. Figure 15 shows a comparison of the predicted aeropropulsive performance (thrust-minus-drag ratio) with the experimental data for both configurations for $M_\infty = 0.90$. The flow that exhausted from the high expansion ratio nozzle (configuration 2) is highly overexpanded and exhibits some internal flow separation at NPR $= 4$, which causes the discontinuity in the trend between NPR $= 4$ and 5 (square symbols, fig. 15). The method predicted the change in performance as the region of nozzle internal flow separation diminished. The predicted thrust-minus-drag ratio was within 0.010 of the experimental data. Considerably higher performance was attained by configuration 4 as the design NPR was bracketed by the NPR range from 5 to 7. The level and trend of the predicted thrust-minus-drag ratio for configuration 4 was within 0.004 of the experimental data in thrust ratio, when the circle symbols are compared with the solid line.

The difference in aeropropulsive performance between configurations 2 and 4 was predicted within 0.005 in thrust ratio for the three NPR settings shown in figure 16. Limitations in calculating the internal flow separation of the turbulence model for configuration 2 likely contributed to the disagreement with the experimental data at NPR $= 5$. The effect on performance of any flow separation, which may be present at NPR $= 6$ and 7, appeared to be less significant than at NPR $= 5$. The comparison of calculated with experimentally determined increments in performance was within 0.002 in thrust ratio for NPR $= 6$ and 7.

Nozzle pressure-drag coefficient. The integrated nozzle pressure-drag coefficient is shown in figure 17. The trend in pressure-drag coefficients with NPR is closely predicted for both configurations, although the absolute level of drag is not well matched. Predicted pressure-drag coefficients for configuration 2 are on the average 0.006 below the experimentally determined pressure-drag coefficients. The opposite condition occurred for configuration 4 where the predicted pressure drag is typically 0.004 above the experimentally determined drag coefficients for the three NPR conditions examined. The lower than predicted drag of configuration 2 was possibly caused by the underprediction of the flow expansion near the nozzle trailing edge. Similarly, the higher than predicted drag of configuration 4 was possibly caused by the overprediction of the expansion on the nozzle boattail shoulder. Accurate pressure drag numbers are sometimes difficult to obtain from wind-tunnel models through the pressure-area integration method. The ability to predict trends, however, is very useful. The prediction of accurate levels of performance may occur with improvements in both testing and computational techniques.

Conclusions

A nozzle internal performance module, which is part of the three-dimensional Navier-Stokes PAB3D method, has been modified to include external aerodynamic flow effects. The flow quantities calculated were external and internal surface static pressure, discharge coefficient, ideal thrust coefficient, thrust-minus-drag ratio, and pressure-drag coefficient. Comparisons of the results of the Navier-Stokes PAB3D method were made with a selection of experimental data from a model of an axisymmetric supersonic cruise nozzle investigation performed in the Langley 16-Foot Transonic Tunnel. Calculations were performed for a single transonic Mach number at several nozzle pressure ratio settings. Solutions for operating conditions close to design and below design nozzle pressure ratios were obtained. The results are summarized as follows:

1. Internal and external surface static-pressure distributions were closely predicted for the selected configurations. In particular, the location of the

internal separation of flow from the divergent section of the high expansion ratio configuration at a nozzle pressure ratio of 4 was predicted closely.

2. Nozzle discharge coefficient was predicted to within 0.5 percent of experimental data for nozzle pressure ratios at design and overexpanded nozzle flow conditions. The trends and the levels of ideal thrust coefficients matched the experimental data well.

3. Thrust-minus-drag ratios were predicted to within 0.010 in thrust ratio. The predicted increment in thrust-minus-drag ratio between the two nozzles for nozzle pressure ratios of 5, 6, and 7 was within 0.005 of the experimental data.

4. Integrated nozzle pressure-drag coefficient trends with nozzle pressure ratio matched fairly closely; however, absolute levels of drag coefficient were not well predicted.

NASA Langley Research Center
Hampton, VA 23681-0001
November 12, 1993

References

1. Carlson, John R.: *A Nozzle Internal Performance Prediction Method.* NASA TP-3221, 1992.

2. Abdol-Hamid, Khaled S.: *Development of Three-Dimensional Code for the Analysis of Jet Mixing Problem—Part I: Laminar Solution.* NASA CR-4200, 1988.

3. Kuchemann, Dietrich; and Weber, Johanna: *Aerodynamics of Propulsion,* First ed. McGraw-Hill Book Co., Inc., 1953.

4. Carson, George T., Jr.; and Lee, Edwin E., Jr.: *Experimental and Analytical Investigation of Axisymmetric Supersonic Cruise Nozzle Geometry at Mach Numbers From 0.60 to 1.30.* NASA TP-1953, 1981.

5. Corson, Blake W., Jr.; Runckel, Jack F.; and Igoe, William B.: *Calibration of the Langley 16-Foot Transonic Tunnel With Test Section Air Removal.* NASA TR R-423, 1974.

6. Newsome, Richard W.; Walters, Robert W.; and Thomas, James L.: An Efficient Iteration Strategy for Upwind/Relaxation Solutions to the Thin-Layer Navier-Stokes Equations. *A Collection of Technical Papers—AIAA 8th Computational Fluid Dynamics Conference,* June 1987, pp. 126 142. (Available as AIAA-87-1113.)

7. Abdol-Hamid, Khaled S.; and Compton, William B., III: Supersonic Navier-Stokes Simulations of Turbulent Afterbody Flows. *A Collection of Technical Papers AIAA 7th Applied Aerodynamics Conference,* July–Aug. 1989, pp. 268–277. (Available as AIAA-89-2194-CP.)

8. Cheatham, P. L.; Walker, S. H.; and Gridley, M. C.: Computation of Vectoring Nozzle Performance. AIAA-90-2752, July 1990.

9. Shapiro, Ascher H.: *The Dynamics and Thermodynamics of Compressible Fluid Flow, Volume I.* Ronald Press Co., 1953.

10. Schlichting, Hermann (J. Kestin, transl.): *Boundary-Layer Theory,* Seventh ed. McGraw-Hill Book Co., 1979.

11. Ames Research Staff: *Equations, Tables, and Charts for Compressible Flow.* NACA Rep. 1135, 1953. (Supersedes NACA TN 1428.)
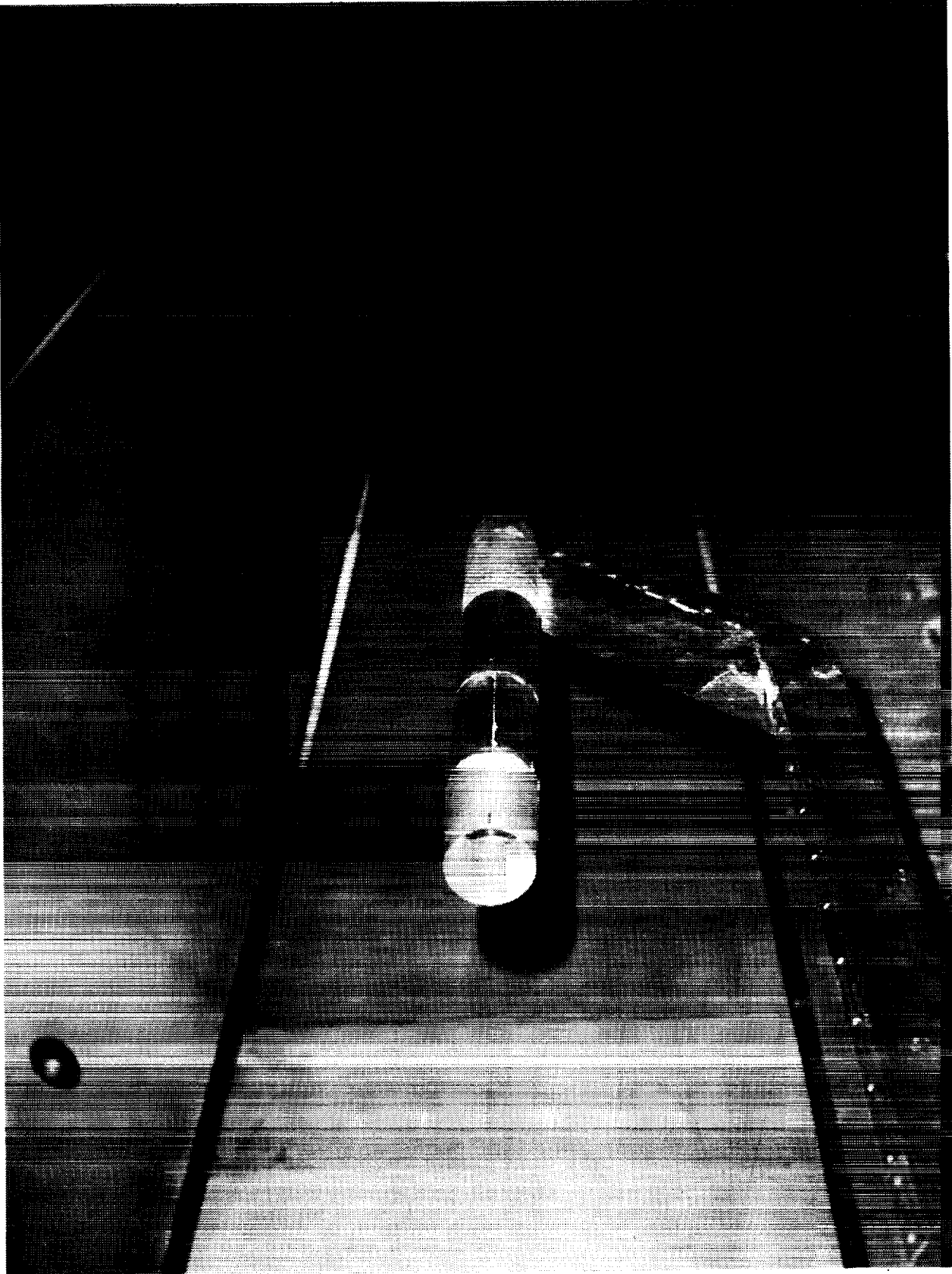
Figure 1. Photograph showing installation of a typical nozzle in test section of Langley 16-Foot Transonic Tunnel.

L-78-5575
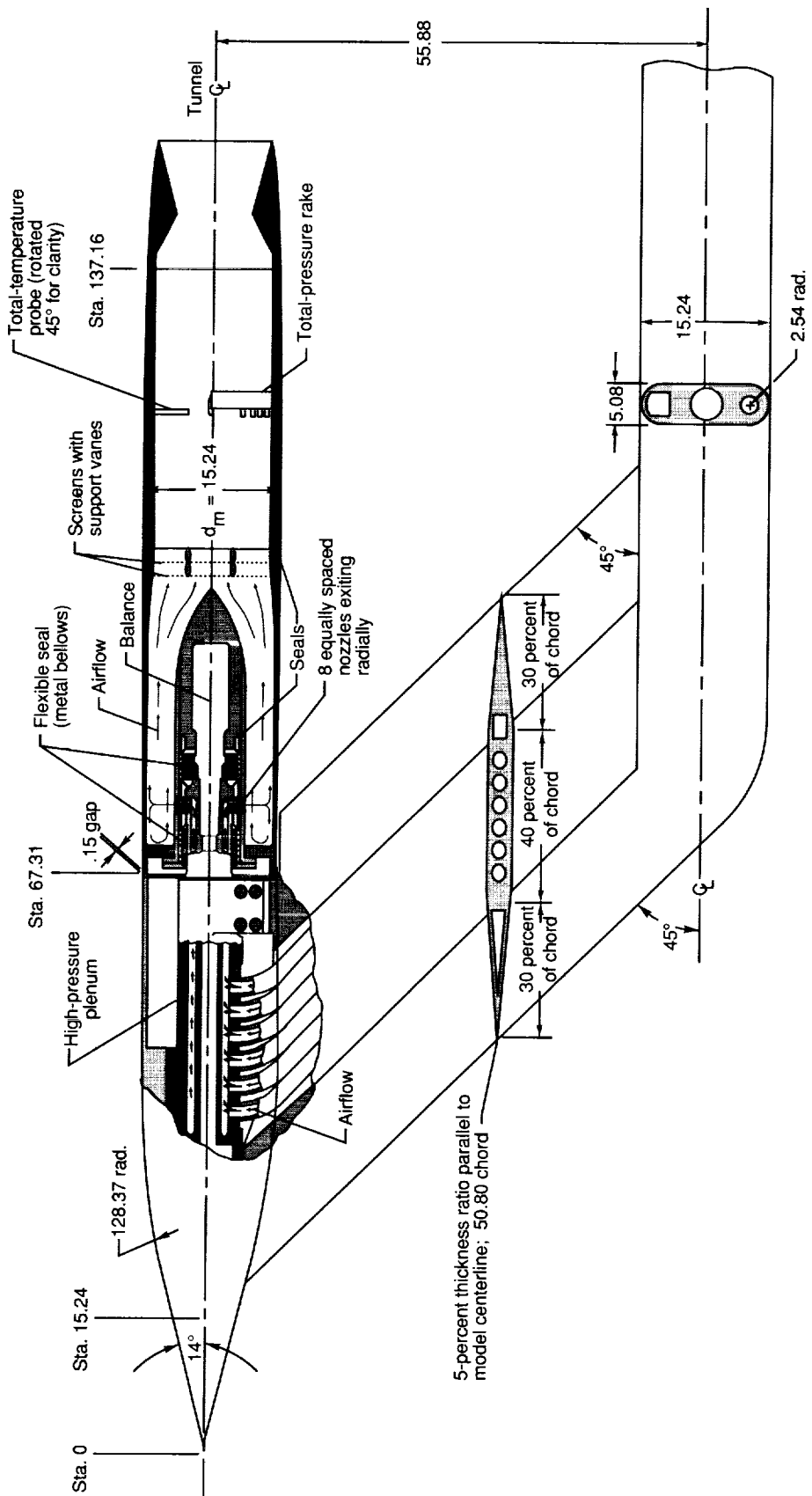
Figure 2. General arrangement of model and support system. All linear dimensions are in centimeters. (From ref. 4.)
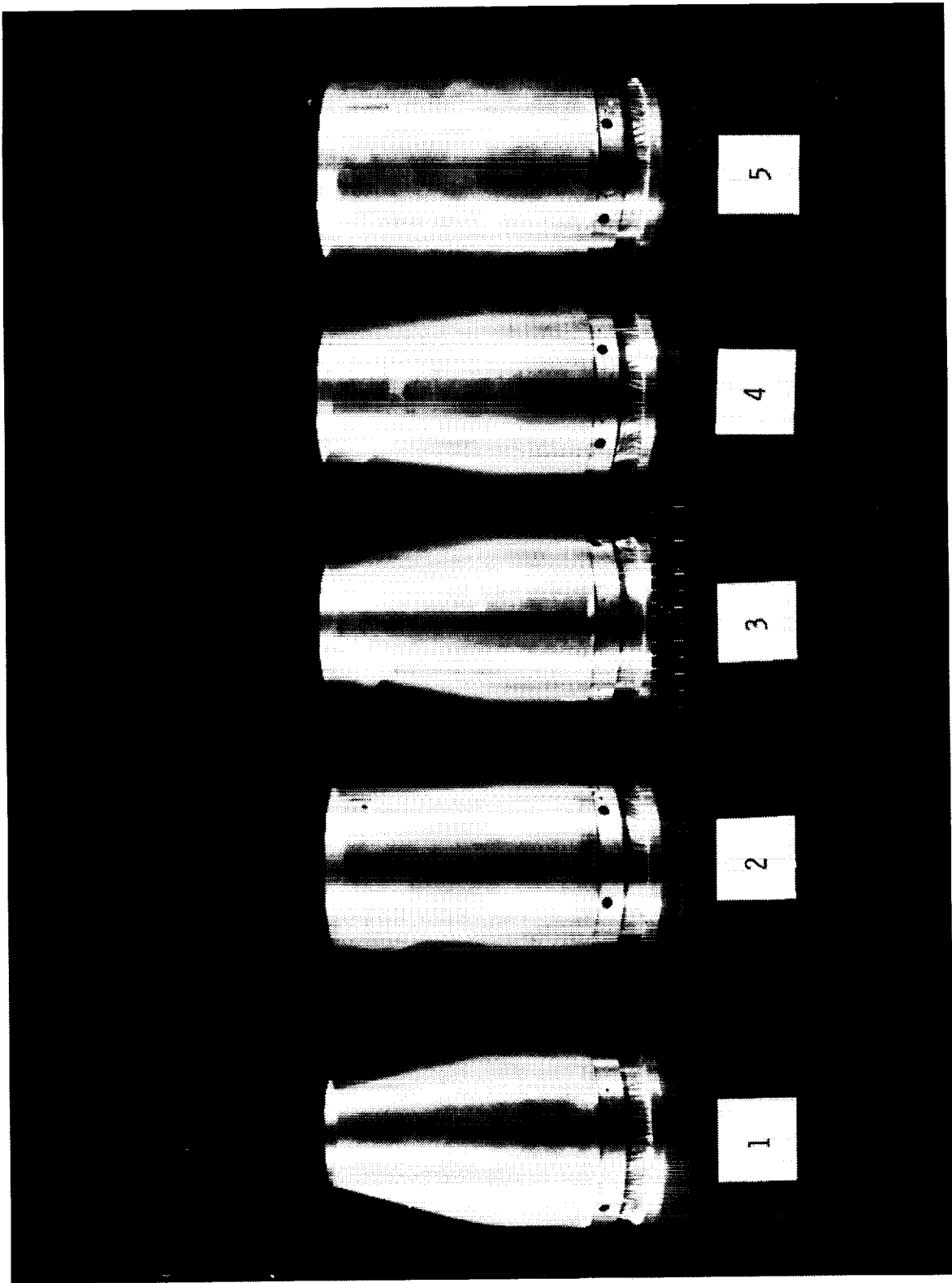
Figure 3. Photograph showing five nozzle configurations tested (ref. 4).

L-78-5750.1

Sta. 137.16

1.303

l

β

.076 (base thickness)

2.540 rad.

22.860 rad.

d_t

d_e

12.863

$d_m = 15.240$

l_C

l_D

1.270 rad.

δ

θ

d_m

x
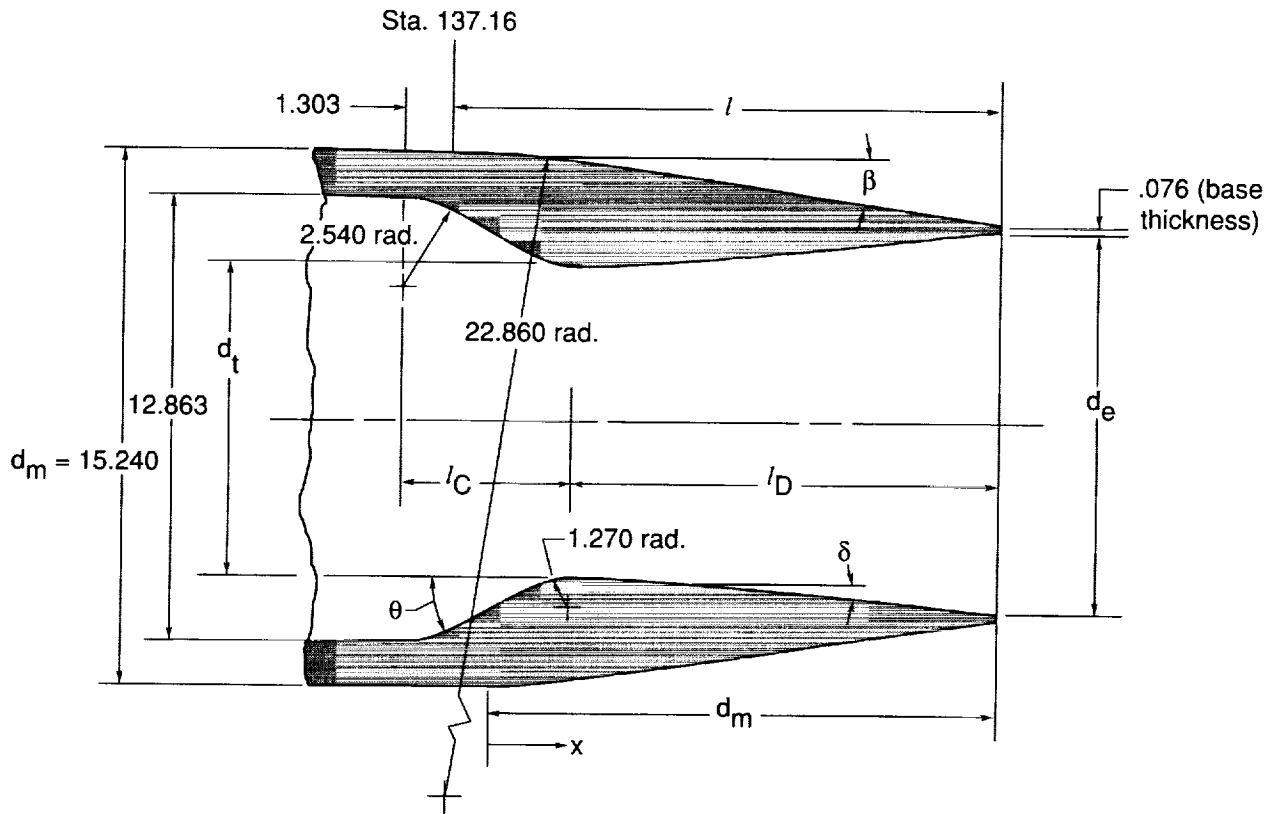
Configuration	Flight segment	Power setting	Design dimensions											
			NPR_{des}	A_e/A_t	A_t/A_m	A_e/A_m	d_t/d_m	l_C/d_m	l_D/d_m	θ, deg	δ, deg	l/d_m	d_e/d_m	β, deg
1	Subsonic cruise	Dry	4.25	1.250	0.250	0.312	0.500	0.286	0.800	42.35	2.12	1.000	0.559	15.05
2	Supersonic cruise	Dry	21.23	3.000	.250	.750	.500	.286	.779	42.35	13.18	.979	.866	3.82
3	Subsonic accel.	Max. dry	5.03	1.350	.300	.405	.548	.299	.799	33.58	3.18	1.012	.636	11.63
4	Transonic accel.	Partial A/B	6.23	1.500	.350	.525	.592	.309	.797	26.90	4.78	1.020	.725	8.28
5	Supersonic accel.	Max. A/B	10.64	2.000	.420	.840	.648	.319	.789	19.58	9.70	1.022	.917	2.12

Figure 4. Geometric details of test nozzle configurations. Absolute linear dimensions are in centimeters.
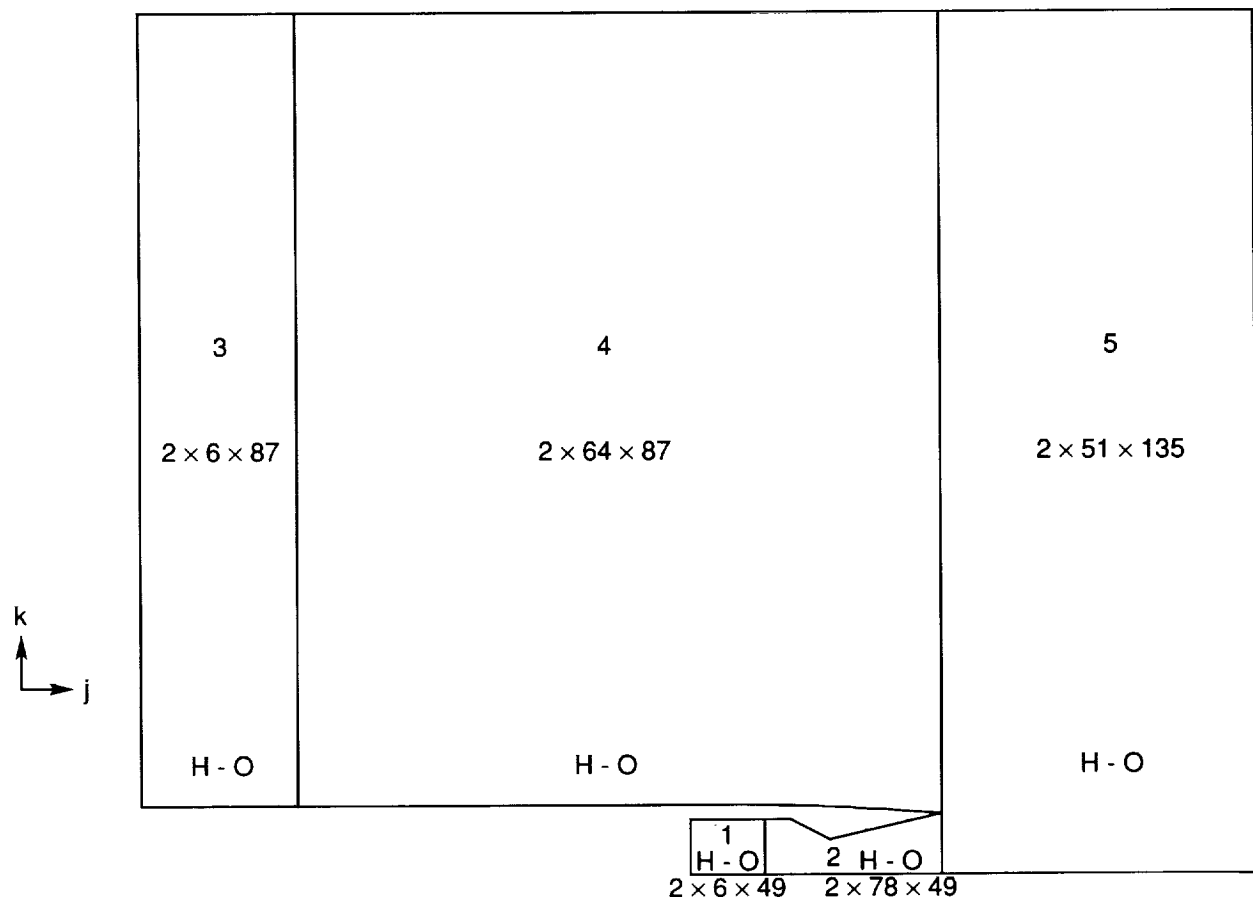
(a) Blocking arrangement and grid dimensions.

Figure 5. Sketch of computational mesh.
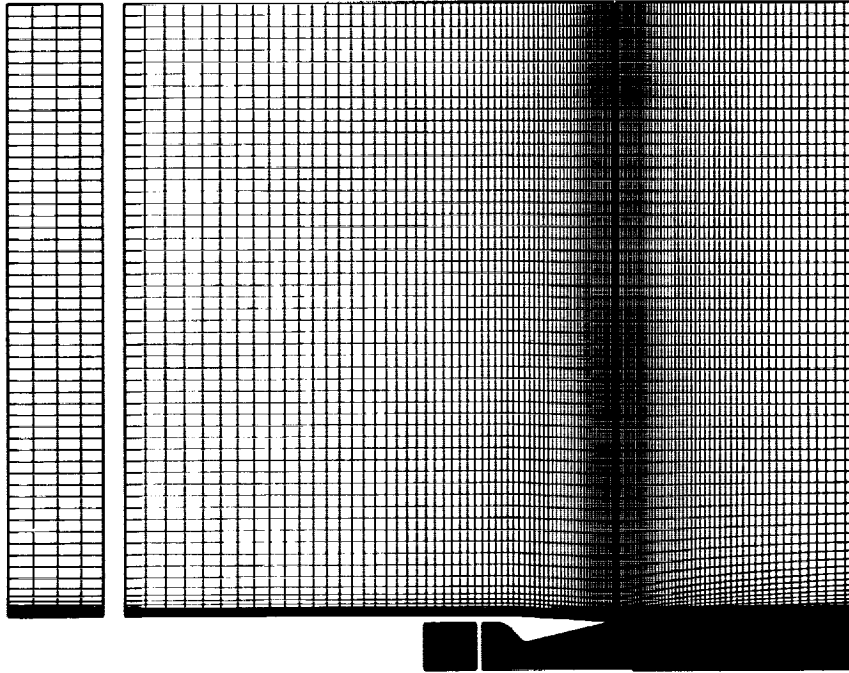
(b) Complete flow field.
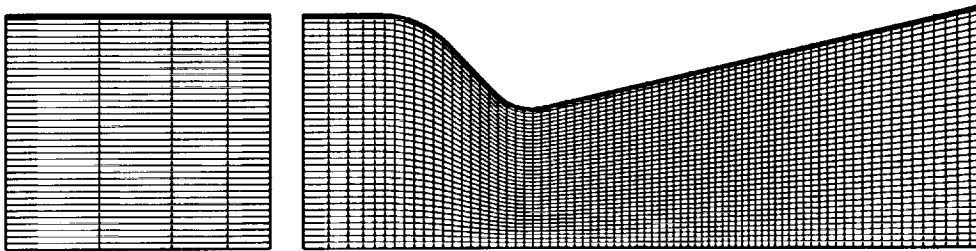
(c) Close-up of nozzle flow path.

Figure 5. Concluded.

14
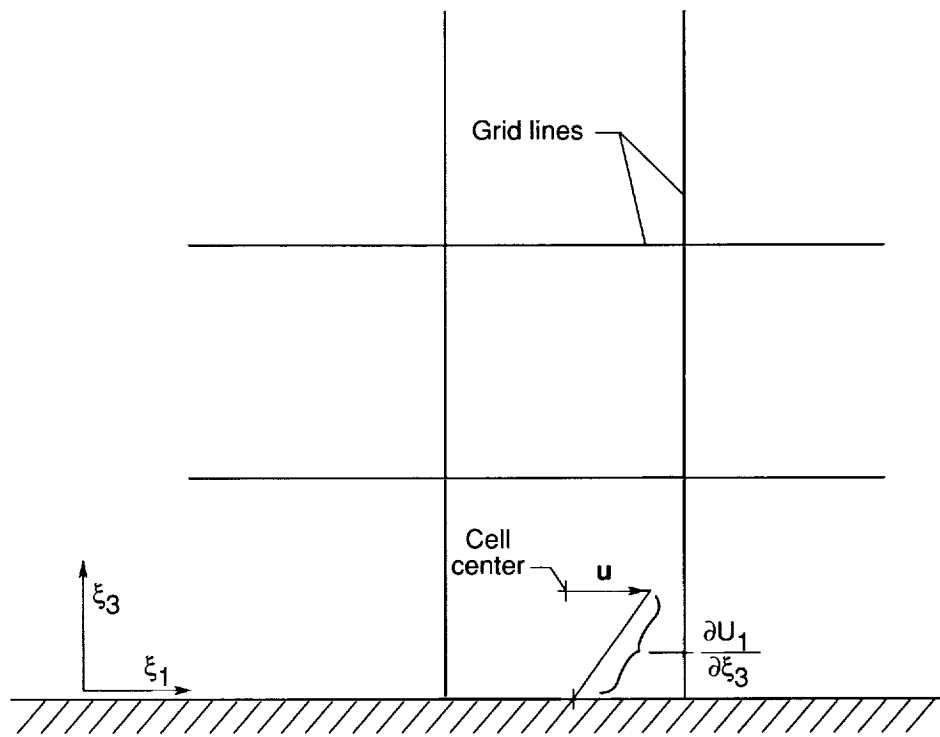
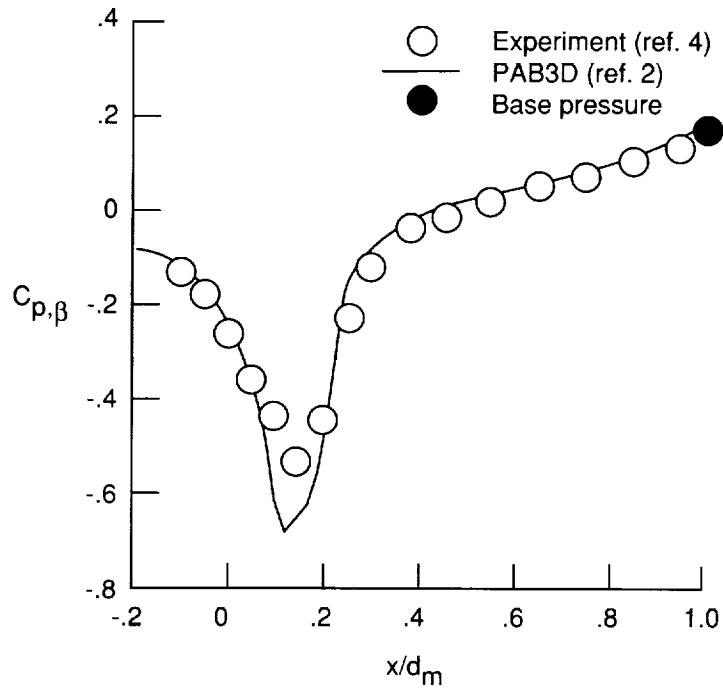Figure 6. Sketch of cell-centered velocity gradient normal to surface.
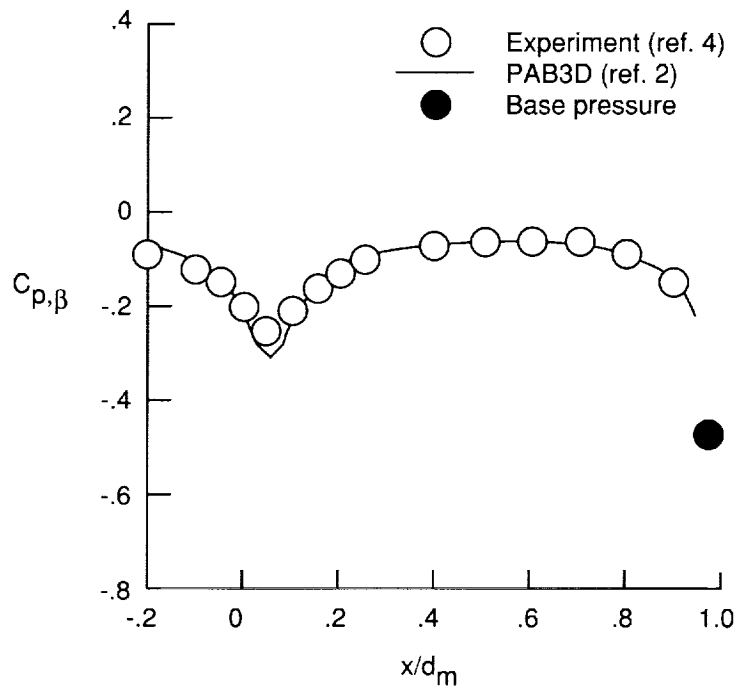
(a) External surface.
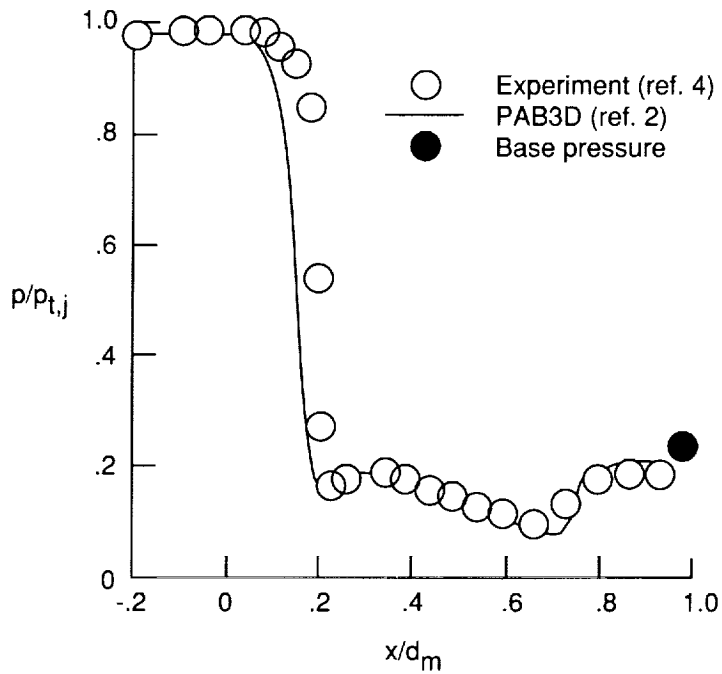
(b) Internal surface.

Figure 7. Comparison of calculation with experimental data for surface-pressure distributions of nozzle configuration 2 with NPR = 4 and $M_\infty = 0.90$.
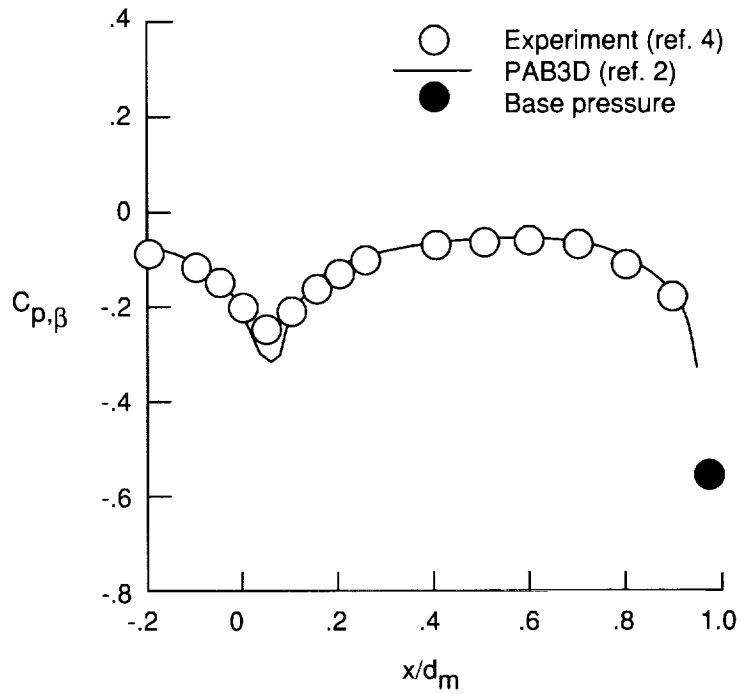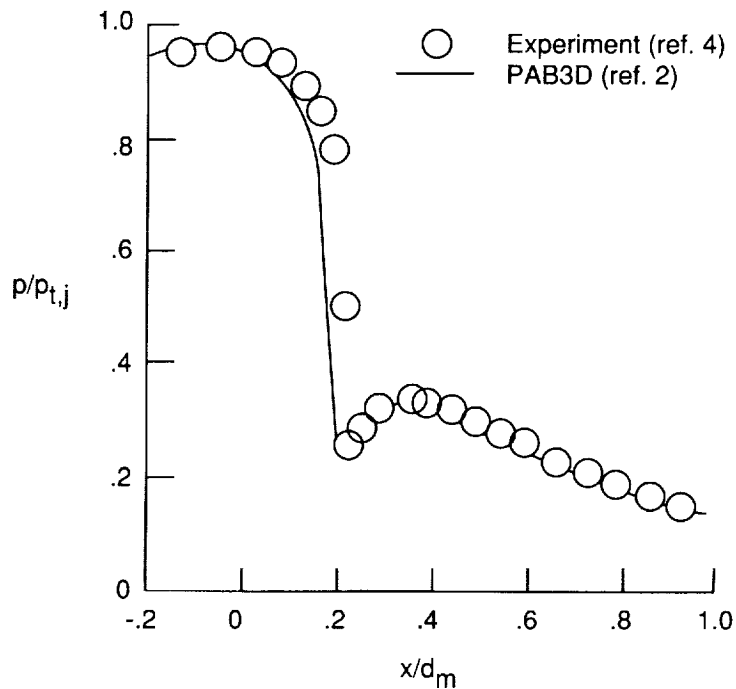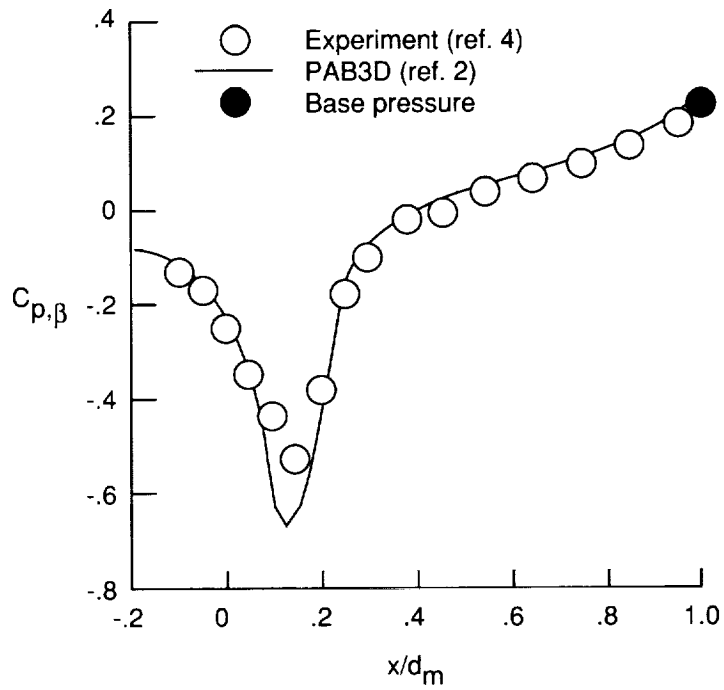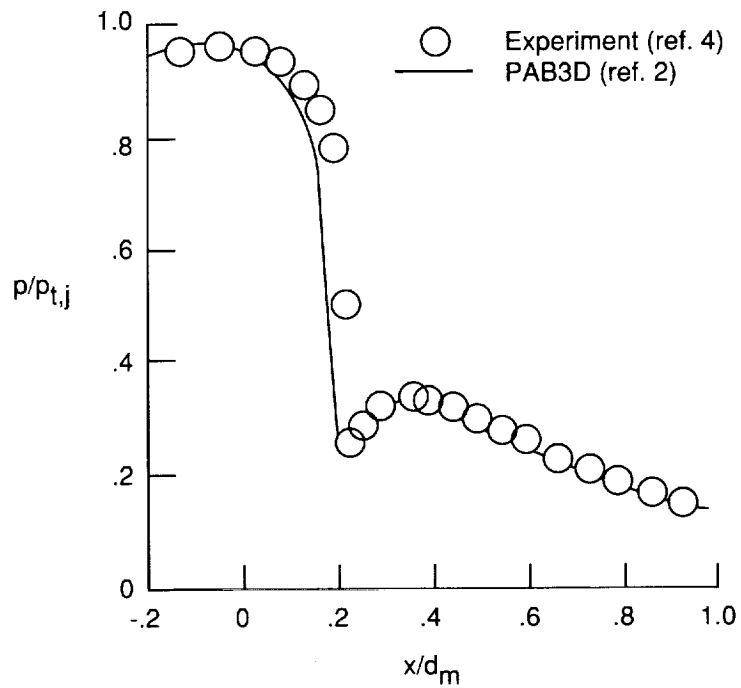
(a) External surface.
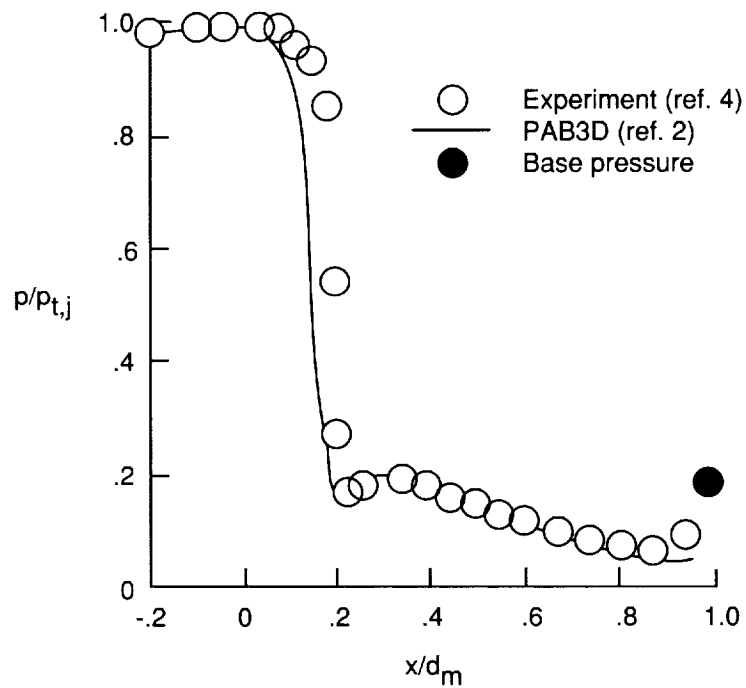
(b) Internal surface.

Figure 8. Comparison of calculation with experimental data for surface-static pressure distributions of nozzle configuration 2 with NPR = 5 and $M_\infty = 0.90$.
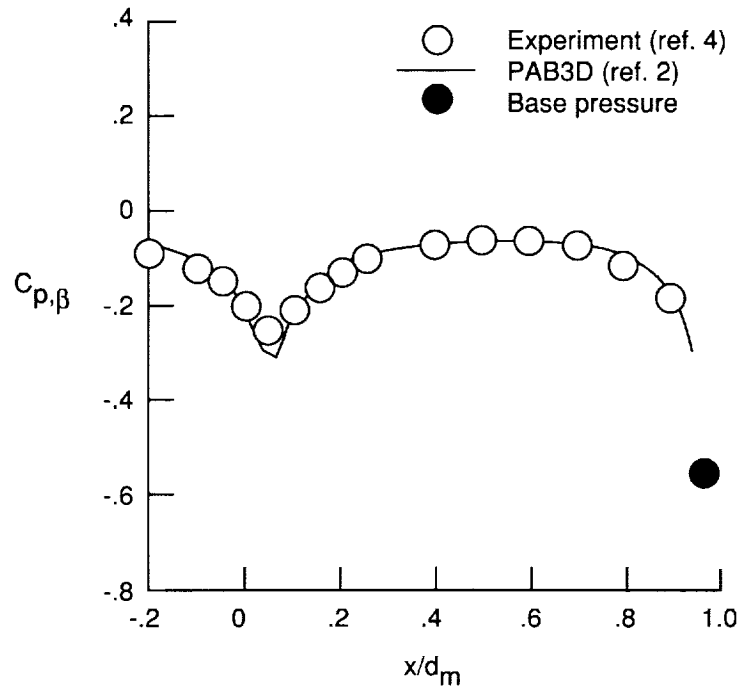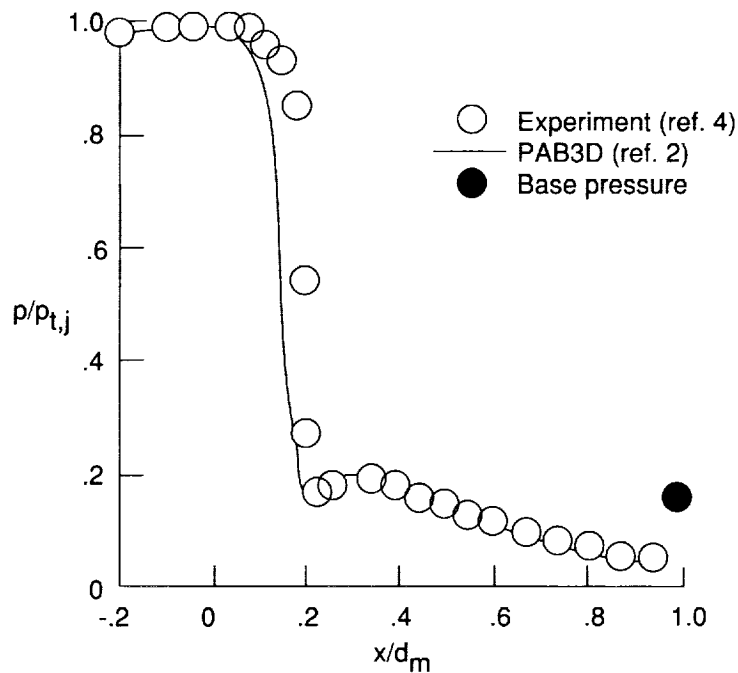
(a) External surface.

(b) Internal surface.

Figure 9. Comparison of calculation with experimental data for surface-pressure distributions of nozzle configuration 2 with NPR = 6 and M_∞ = 0.90.
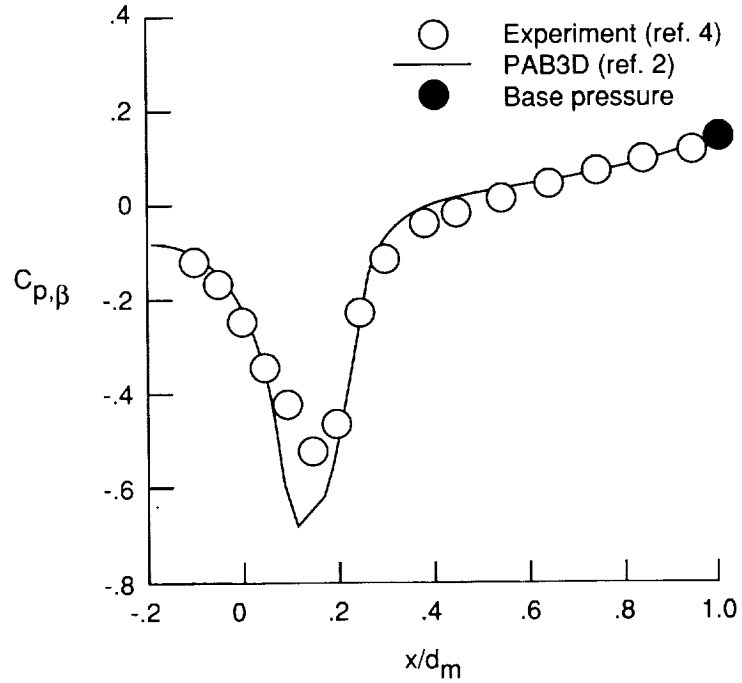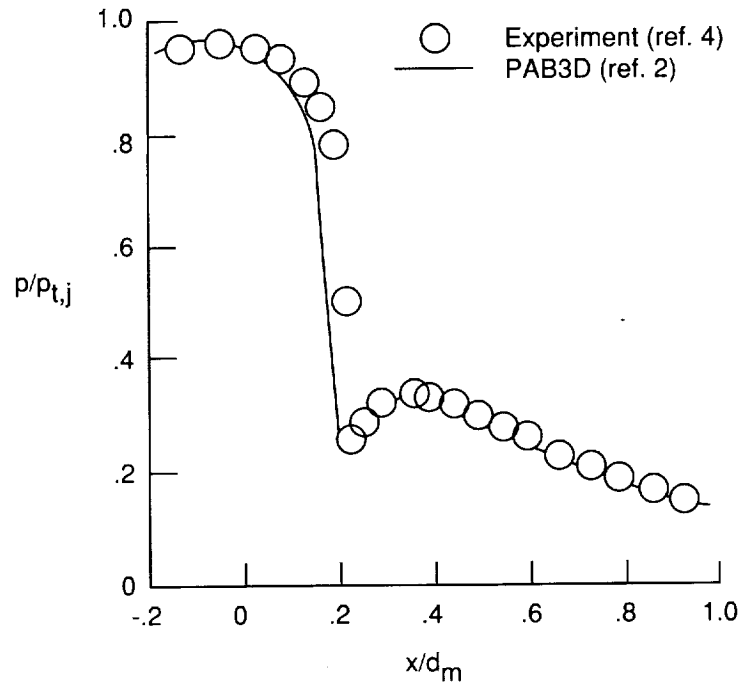
(a) External surface.

(b) Internal surface.

Figure 10. Comparison of calculation with experimental data for surface-pressure distributions of nozzle configuration 4 with NPR = 5 and $M_\infty = 0.90$.

(a) External surface.

(b) Internal surface.

Figure 11. Comparison of calculation with experimental data for surface-pressure distributions of nozzle configuration 4 with NPR = 6 and $M_\infty = 0.90$.

(a) External surface.

(b) Internal surface.

Figure 12. Comparison of calculation with experimental data for surface-pressure distributions of nozzle configuration 4 with NPR = 7 and $M_\infty = 0.90$.
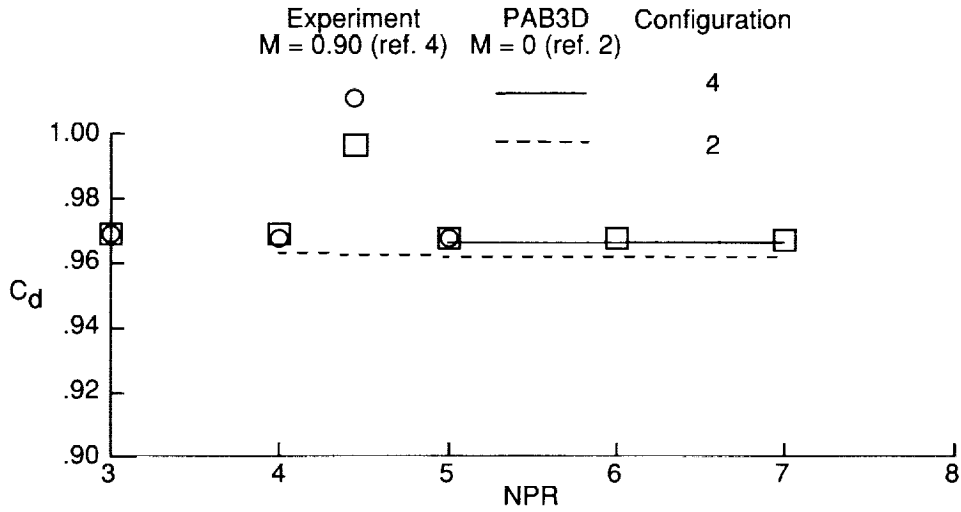
Figure 13. Comparison of calculation with experimental data for nozzle discharge coefficients.
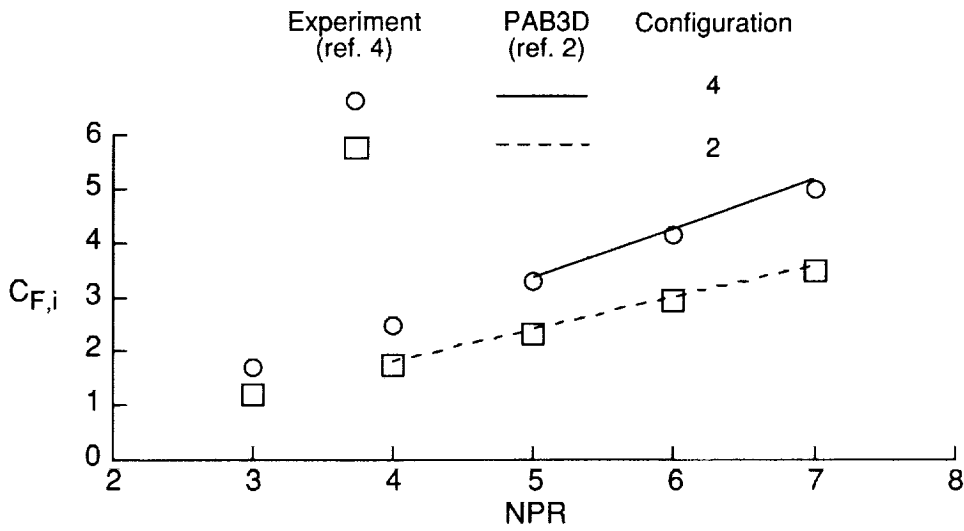
Figure 14. Comparison of calculation with experimental data for variation in nozzle ideal thrust coefficient with NPR with $M_\infty = 0.90$ and $\alpha = 0°$.
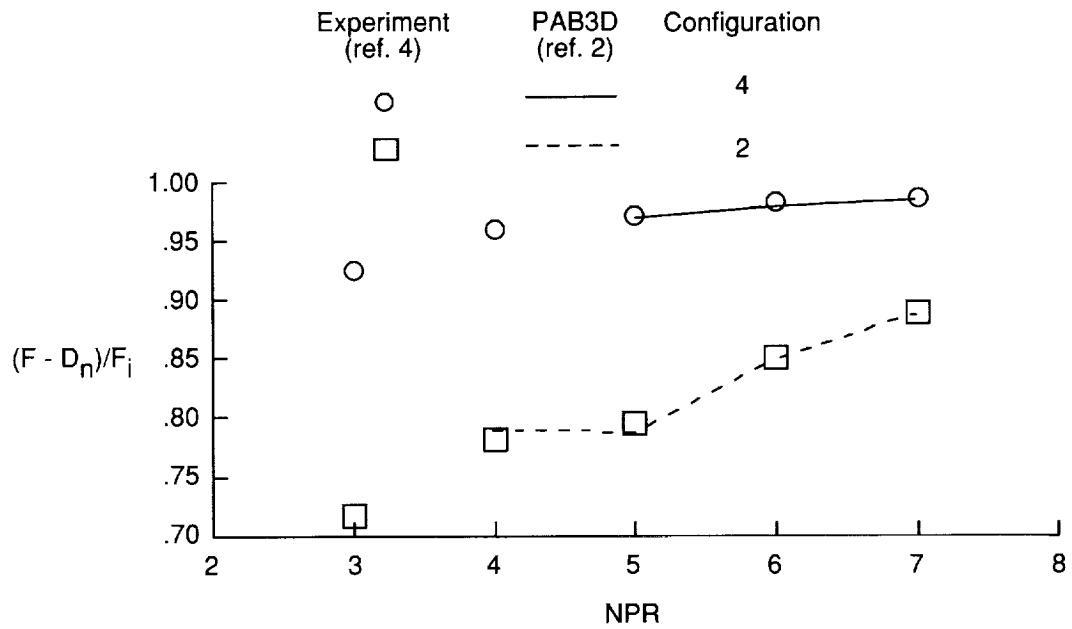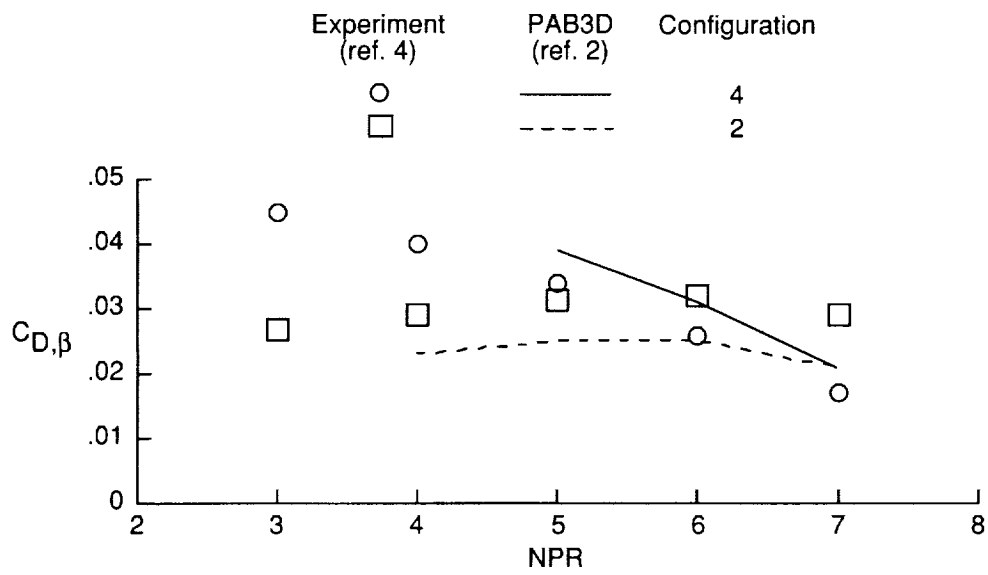
Figure 15. Comparison of calculation with experimental data for variation in aeropropulsive performance with NPR with $M_\infty = 0.90$ and $\alpha = 0°$.
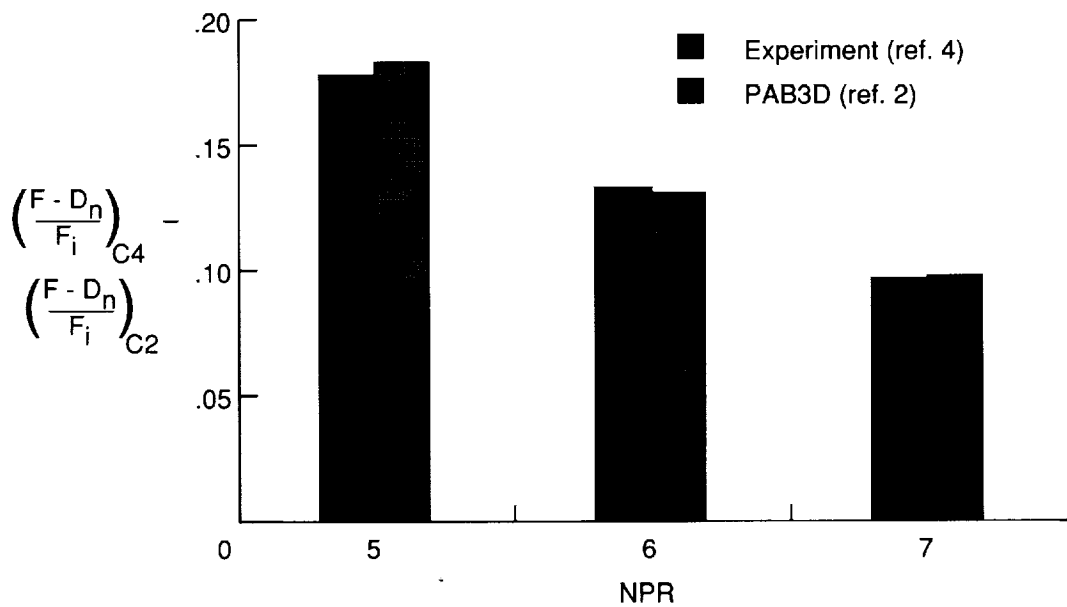
Figure 16. Comparison of calculation with experimental data for variation of increment in aeropropulsive performance with nozzle configuration.
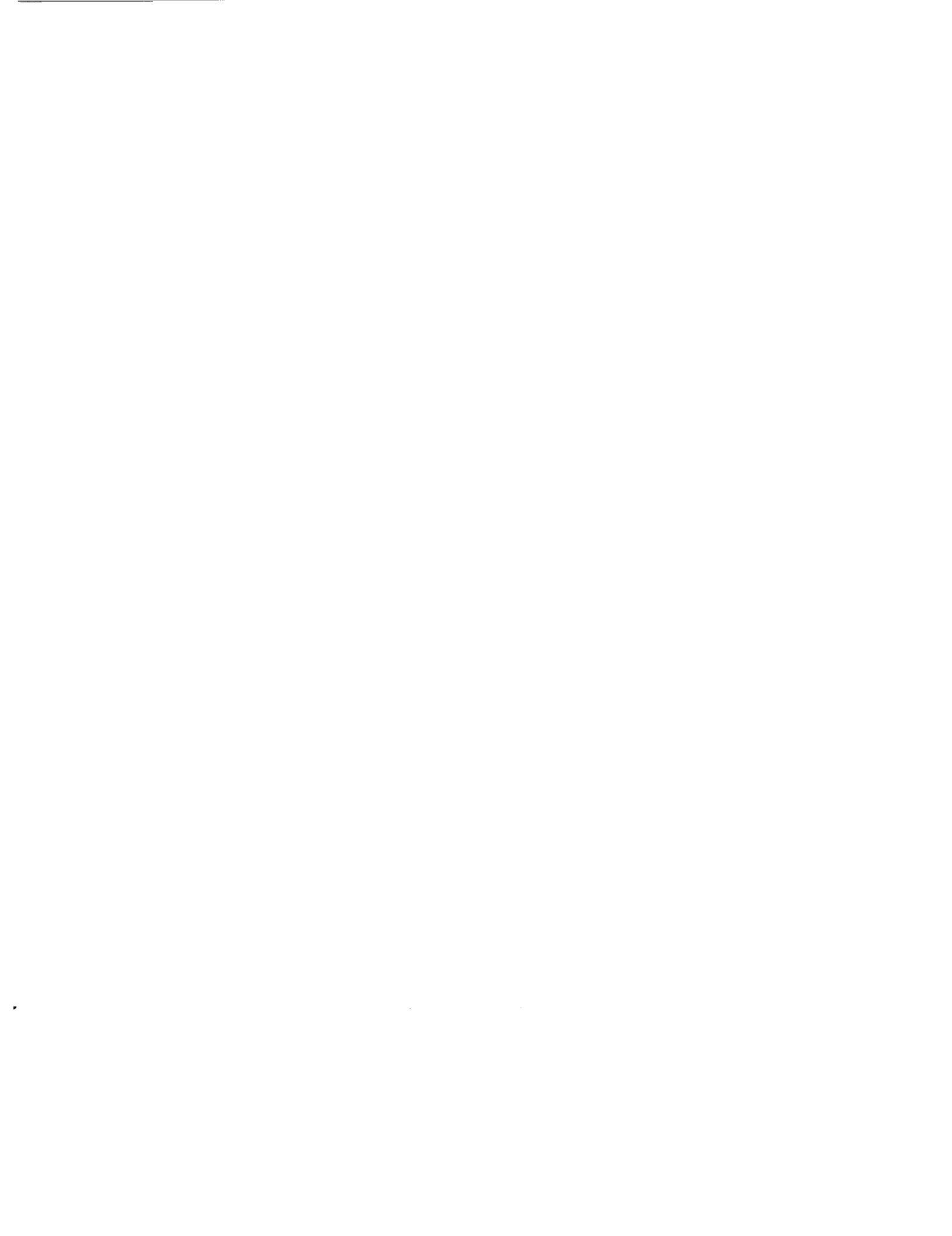
23

Figure 17. Comparison of calculation with experimental data for variation of integrated nozzle pressure drag with NPR with $M_\infty = 0.90$ and $\alpha = 0°$.

REPORT DOCUMENTATION PAGE

1. AGENCY USE ONLY*(Leave blank)*	2. REPORT DATE February 1994	3. REPORT TYPE AND DATES COVERED Technical Memorandum

4. TITLE AND SUBTITLE
Computational Prediction of Isolated Performance of an Axisymmetric Nozzle at Mach Number 0.90

5. FUNDING NUMBERS
WU 505-62-30-01

6. AUTHOR(S)
John R. Carlson

7. PERFORMING ORGANIZATION NAME(S) AND ADDRESS(ES)
NASA Langley Research Center
Hampton, VA 23681-0001

8. PERFORMING ORGANIZATION REPORT NUMBER
L-17248

9. SPONSORING/MONITORING AGENCY NAME(S) AND ADDRESS(ES)
National Aeronautics and Space Administration
Washington, DC 20546-0001

10. SPONSORING/MONITORING AGENCY REPORT NUMBER
NASA TM-4506

11. SUPPLEMENTARY NOTES

12a. DISTRIBUTION/AVAILABILITY STATEMENT

Unclassified–Unlimited

Subject Category 02

12b. DISTRIBUTION CODE

13. ABSTRACT *(Maximum 200 words)*
An improved ability to predict external propulsive performance has been incorporated into the three-dimensional Navier-Stokes code PAB3D. The improvements are the ability to account for skin friction and external pressure forces. Performance parameters for two axisymmetric supersonic cruise nozzle configurations were calculated to test the improved methodology. Internal and external flow-field regions were computed using a two-equation k-ϵ turbulent viscous-stress model. The computed nozzle discharge coefficient matched the experimental data within 0.5 percent in both level and trend. The calculated thrust-minus-drag ratios were within 1 percent of the absolute level of experimental data and the trends of data were predicted accurately. The predicted trend of integrated nozzle pressure drag matched the trend of the integrated experimental pressure drag over a range of nozzle pressure ratios, but absolute drag levels were not accurately predicted.

14. SUBJECT TERMS
Nozzle; Navier-Stokes; Computational fluid dynamics; Transonic flow; Supersonic cruise; Isolated performance; Performance prediction

15. NUMBER OF PAGES
25

16. PRICE CODE
A03

17. SECURITY CLASSIFICATION OF REPORT Unclassified	18. SECURITY CLASSIFICATION OF THIS PAGE Unclassified	19. SECURITY CLASSIFICATION OF ABSTRACT	20. LIMITATION OF ABSTRACT